Journal of Materials Chemistry A

In-situ Al_2O_3 Incorporation Enhances the Efficiency of $CuIn(S,Se)_2$ Solar Cells Prepared from Molecular-Ink Solutions

Journal:	*Journal of Materials Chemistry A*
Manuscript ID	TA-ART-01-2021-000768.R1
Article Type:	Paper
Date Submitted by the Author:	23-Mar-2021
Complete List of Authors:	Septina, Wilman; University of Hawaii, Hawaii Natural Energy Institute Muzzillo, Christopher; National Renewable Energy Laboratory Perkins, Craig; National Renewable Energy Laboratory, Curtis Giovanelli, Anne; University of Hawaii, Hawaii Natural Energy Institute West, Thomas; University of Hawaii, Hawaii Natural Energy Institute Ohtaki, Kenta; University of Hawaii, Hawai'i Institute of Geophysics & Planetology Ishii, Hope; University of Hawaii, Hawai'i Institute of Geophysics & Planetology Bradley, John; University of Hawaii, Hawai'i Institute of Geophysics & Planetology Zhu, Kai; National Renewable Energy Laboratory, Chemical and Materials Science Center Gaillard, Nicolas; University of Hawaii, Hawaii Natural Energy Institute

In-situ Al_2O_3 Incorporation Enhances the Efficiency of $CuIn(S,Se)_2$ Solar Cells Prepared from Molecular-Ink Solutions

*Wilman Septina,[1] Christopher P. Muzzillo,[2] Craig L. Perkins,[2] Anne Curtis Giovanelli,[1] Thomas West,[1] Kenta K. Ohtaki,[3] Hope A. Ishii,[3] John P. Bradley,[3] Kai Zhu,[2] Nicolas Gaillard.[1]**

[1]Hawaii Natural Energy Institute, University of Hawaii, 1680 East-West Rd POST 109, Honolulu, HI 96822

[2]National Renewable Energy Laboratory, 15013 Denver W Pkwy, Golden, CO 80401

[3]Hawaii Institute of Geophysics & Planetology, University of Hawaii, Honolulu, Hawaii 96822, USA

***Corresponding Author**

E-mail: ngaillar@hawaii.edu

Abstract

We report an efficiency enhancement of solution-processed $CuIn(S,Se)_2$ (CISSe) thin film solar cells via in-situ incorporation of Al_2O_3. These films were produced using inks containing CuCl, $InCl_3$, $AlNO_3$ (Al/Al+In: 0.1) and thiourea dissolved in methanol. After spin coating of these solutions in air, samples were subjected to a selenization process. Auger electron spectroscopy depth-profiling analysis showed that Al is evenly distributed throughout the bulk of the film. Transmission electron microscopy revealed that $AlNO_3$ precursor reacted with oxygen to form nanosized amorphous Al_2O_3 grains located within the bulk and grain boundaries of CISSe, as well as at both the top and bottom interfaces. Power conversion efficiency (PCE) as high as 11.6% (J_{SC}: 35.8 mA cm^{-2}, V_{OC}: 518 mV, FF: 62.2%, no anti-reflection coating) was achieved with Al-CISSe solar cell devices integrated with CdS (chemical bath deposition, thickness: 80 nm) and ZnO/ITO bilayers (sputtered, thickness: 300 nm). The average PCE (10.1%, $<J_{SC}>$: 34.5 mA cm^{-2}, $<V_{OC}>$: 491 mV, <FF>: 59.8%) was nearly 4% (absolute) higher than that measured on CISSe baseline cells fabricated from solutions without Al (<PCE>=6.4%, $<J_{SC}>$: 32.8 mA cm^{-2}, $<V_{OC}>$: 410 mV, <FF>: 47.3%). This in-situ Al_2O_3 incorporation is speculated to play a role in the enhancement of the V_{OC} and FF of the devices through passivation of defects in CISSe reducing interface and bulk recombination, as evidenced by a reduced defect density and an increased activation energy of the dominant recombination mechanism from capacitance and temperature-dependent V_{OC} measurements, respectively.

Keywords: chalcopyrite, molecular ink, Al_2O_3, passivation, photovoltaics

1. Introduction

Thin film solar cells, in particular $CuInGaSe_2$ (CIGSe) chalcopyrites, offer some of the most efficient materials for light conversion to electricity with relatively low raw materials usage and

production costs compared to crystalline Silicon (c-Si). As of 2019, CIGSe record efficiency has achieved 23.4% efficiency,[1,2] a value comparable to that achieved with c-Si solar cells. Despite these attributes, the market share of CIGSe photovoltaics is still relatively low, below 2%.[3] In principle, numerous pathways exist to elevate chalcopyrite photovoltaics to be more competitive and appealing in the energy market, including increasing cell efficiency, increasing module durability, lowering fabrication costs, and/or selecting cheaper constituents.

In recent years, passivating CIGSe surfaces with dielectric materials to further boost efficiency has gained a lot of attention.[4,5] In particular, coating CIGSe with a thin layer of Al_2O_3 using atomic layer deposition (ALD) processes was shown to decrease interface recombination and resulted in improved efficiency,[4-8] a strategy borrowed from silicon solar cell technologies where dielectric passivation layers (SiN_x, SiO_2, Al_2O_3) are applied at the front or rear surfaces of the silicon wafer.[9,10] Passivation with Al_2O_3 has also been applied successfully to other thin film absorbers such as $Cu_2ZnSnSe_4$ (CZTSe) and CdTe,[11-14] leading to chemical and/or field-effect passivations.[15-19] For chemical passivation, Al_2O_3 layers have been shown to reduce the total number of electrically active defects at the semiconductor surface, which in turn lowers surface recombination velocities. For field-effect passivation, since the passivating materials have high-densities of fixed charge, a built-in electric field is created at the semiconductor surface, driving minority carriers into the space-charge region.

In this paper, we report for the first time on an in-situ incorporation of Al_2O_3 in solution-processed $CuIn(S,Se)_2$ (CISSe) thin film solar cells with significant efficiency enhancement. These films were produced using inks containing CuCl, $InCl_3$, $AlNO_3$ (Al/Al+In: 0.1) and thiourea dissolved in methanol. The inks were spin coated onto molybdenum-coated glass substrates in air, followed by a selenization step. Instead of alloying directly with CISSe, our study showed that Al formed

amorphous nanosized-Al_2O_3 covering parts of the film top and bottom surfaces as well as embedded into the bulk. Power conversion efficiency (PCE) as high as 11.6% was measured on Al-CISSe solar cell devices, a value significantly higher than that measured on CISSe baseline cells fabricated with an identical process but without Al (PCE of champion cell: 8.3%). This PCE improvement, which stemmed primarily from an increase in both open-circuit voltages (V_{OC}) and fill factors (FF), confirms the beneficial contribution of Al_2O_3 to defect passivation. By eliminating the need for an extra deposition step in a vacuum chamber before or after the absorber synthesis, this in-situ incorporation technique greatly simplifies processing and could be extended to several absorber classes and other dielectric passivation layers, such as SiO_2.

2. Experimental Section

2.1 Experimental

Ink fabrication: The Al-containing ink precursor was made by sequential addition of 0.30 M (0.164 g) $InCl_3$ (99.999%, Sigma Aldrich), 0.03 M (0.028 g) $AlNO_3$ (99.997%, Sigma Aldrich), 1.77 M (0.337 g) thiourea (≥99.0%, Sigma Aldrich), and 0.26 M (0.064 g) CuCl (≥99.995%, Sigma Aldrich) into 2.5 ml of methanol (≥99.0%, Sigma Aldrich). The metallic ratios of the Al-containing ink were Cu/(In+Al)=0.8, Al/(Al+In)=0.1, and thiourea/(Cu+In+Al)=3.0. The ink was ultrasonicated for 10 minutes between the addition of each chemical. After the addition of CuCl, the ink was stirred at 65 ^oC for 30 min until a clear solution was obtained. Apart from the addition of $InCl_3$ which was done in N_2-filled glove box (O_2<0.1 ppm, moisture<0.5 ppm), all other chemicals were added in air. The Al-free CISSe ink precursor was made following the same recipe, except than no $AlNO_3$ was added to the solution (Cu/In=0.8, thiourea/(Cu+In)=3.0.

Absorber fabrication: Inks were deposited by spin coating onto soda-lime glass substrates coated with DC-sputtered 800 nm thick Mo films. Prior to spin coating, the Mo substrates were further cleaned by consecutive sonication in acetone, methanol, and deionized water, each for 10 min, and then followed with drying under N_2 stream. Inks were filtered with a 0.45 μm syringe-filter (Minisart RC25). In the spin coating deposition, 80 μl of ink was dropped onto the substrate and spun at 2000 rpm for 45 s. The spin-coated film was then annealed for 3 min on a hot plate set at 350 ^oC (actual sample surface temperature at equilibrium: 250 ^oC) and allowed to cool down naturally. Both the coating and annealing were performed in air. These processes were repeated 10 times to increase thickness. The as-deposited film was then placed into a vacuum furnace in the presence of 50 mg Se powder. The furnace was evacuated and purged with N_2 three times and finally backfield with N_2 at 300 mtorr. Samples were first heated at 100^oC for 30 min to remove any leftover solvent, and finally selenized at 550 ^oC for 10 min (ramping rate of 25 ^oC/min), before cooling naturally to room temperature.

Solar cell preparation: No KCN etching was performed on the absorbers prior to device fabrication. An 80 nm CdS layer was deposited onto the absorbers by chemical bath deposition (CBD). In a typical CBD process, a solution containing mixture of $CdSO_4$ (0.015 M), NH_4OH (7.2 M), and thiourea (1.5 M) dissolved in deionized water was poured into a water bath previously heated at 85 ^oC, followed by immersion of the absorbers for 8 min. The CdS-coated absorbers were then annealed in air for 7 min in a laboratory oven (FisherScientific Isotemp 500 Series) set at 120 ^oC. The solar cell devices were completed with RF-sputtered of undoped ZnO (i-ZnO, room temperature, 200 nm) and In_2O_3/SnO_2 90/10 wt% (ITO, 200 ^oC, 100 nm). The total area of each cell (0.12 cm^2) was defined by the

diameter of circular holes of the shadow mask used during the ITO deposition. No metallic grids nor anti reflective coatings were used in this experiment. All cells underwent an additional 2-minute long heat treatment in air on a hot plate set at 225 ^{o}C (actual sample surface temperature at equilibrium: 150 ^{o}C).

2.2 Characterization

Ink and film characterization: Thermogravimetric and differential scanning calorimetry (TG-DSC) analysis of the liquid inks was performed using a TA instrument Q600 simultaneous TG/DSC instrument at a heating rate of 5 ^{o}C/min to 600 ^{o}C under nitrogen flow (100 ml/min). Morphologies of the films were examined using a Hitachi S-4800-I field emission scanning electron microscope (FE-SEM). Crystal structures of the fabricated films were evaluated by X-ray diffraction (XRD) using a Bruker D8 Advance X-ray diffractometer equipped with a copper cathode outputting a wavelength of 1.54056 Å. Raman spectra were obtained using a confocal Raman microscope (Witec, alpha R300) equipped with a 532 nm laser. Cross section elemental maps were generated via energy dispersive x-ray spectroscopy (EDX, 10 kV, 3.2 nA) using a Helios NanoLab 660 dual-beam focused ion beam instrument (FIB-SEM, FEI/Thermo Fisher) equipped with an X-max N80 SDD-EDX detector (Oxford Instruments). A trench was milled using a 30 kV Ga^{+} focused ion beam and EDX maps taken on the exposed cross section surface. Additionally, an electron transparent thin section was prepared using the FIB-SEM for subsequent scanning transmission electron microscope (STEM) analyses. STEM images and EDX measurements (300 kV) were conducted on a High-base Titan G2 (Scanning) Transmission Electron Microscope (FEI/Thermo Fisher) equipped with a solid-state Si(Li) EDX detector (Genesis 4000, EDAX).

Auger electron spectroscopy (AES) depth-profiles were measured using a Physical Electronics PHI 670 scanning Auger microscope with a 5 kV, 20 nA electron beam and a 3 kV beam of Ar^+ for sputtering. Auger results were quantified using sensitivity factors derived from a CIGSe film of known composition according to a previously described procedure.[20] Default sensitivity factors were used for aluminum, sulfur, molybdenum, and oxygen. AES was chosen over EDX to characterize Al-containing samples since the X-ray spectra of Al and Se exhibit some overlap (Al-Kα: 1.486, Se-Lα: 1.379). Diffuse reflectance measurement was performed using a Perkin Elmer Lambda 750S spectrometer equipped with an integrating sphere.

Solar cell characterization: Current density–voltage (J-V) curves of the solar cell devices were measured using a temperature-controlled stage at 25 ^oC under simulated AM 1.5_G irradiation provided by a 1000 W solar simulator equipped with a Xe bulb and an AM1.5G filter (Newport, 91192-1000). The power output of the solar simulator was adjusted using an NREL-calibrated Si photodiode. The ITO was contacted with indium-coated Kelvin probes. External quantum efficiency (EQE) was measured with a 75 W Xe lamp focused to a 1 mm × 2.5 mm beam area chopped at 31 Hz. Temperature-dependent open circuit voltage (V_{OC}-T) were performed using a cryostat cooled with liquid-He and equipped with a Lake Shore 335-temperature controller. The devices were illuminated using a white LED lamp which illumination (1 sun) was adjusted until the devices short-circuit current density (J_{SC}) matched that measured with the 1000W solar simulator (AM1.5_G illumination). Capacitance-voltage (C-V) measurements were performed at room temperature in dark at 10 kHz and AC voltage of 50 mV using a Biologic SP-200 potentiostat equipped for impedance analysis. The DC bias voltage was swept from 0.6 to -1.5 V, and carrier concentration was extracted using a dielectric constant of 13.6.

3. Results and Discussion

TG-DSC analyses were performed to the Al-containing ink to understand its thermal decomposition behavior (**Fig. 1**). In the low temperature region (<100 ^{o}C), DSC showed an endothermic peak at 37.5 ^{o}C coinciding with a significant weight loss from TG (~60%), corresponding most likely to the evaporation of methanol. The loss of methanol prior to its boiling point (64.7 ^{o}C) should be caused by its high volatility coupled with the fact that the measurement was performed from a small amount of sample under nitrogen gas flow. Further weight loss was observed in the TG up to 100 ^{o}C (~10%) accompanied by weak endothermic peaks between 88.7 ^{o}C and 105 ^{o}C, presumably caused by the evaporation of residual water dissolved in the solvent. Further weight loss with an endothermic peak at 223.5 ^{o}C was detected, which is the typical decomposition temperature of thiourea (TU) and metal-TU complexes preceding the formation of $CuInS_2$.[21-23] It has been reported that the metal cations are stabilized as metal-TU complexes (e.g., $Cu(TU)_3Cl$, $In(TU)_3Cl_3$) in the presence of TU for a wide range of solvents,[24-26] and the formation of $CuInS_2$ nanocrystalline domains was proposed to proceed through thermal decomposition of those complexes.[23] The endothermic peak of 294.6 ^{o}C accounting for 3% mass loss from the TG is presumed to be caused by regeneration of HNCS gases.[21] Above this temperature, a gradual decrease of the mass was detected, which was caused by decomposition of the leftover hydrocarbon in the ink. It is worth noting that DSC from the aluminum-containing ink showed a weak exothermic peak at 503 ^{o}C which was not observed from the Al-free ink (**Fig. S1**). As a reference, Ito et al. showed a formation of $CuIn_xAl_{1-x}S_2$ by sulfurizing metallic precursors above 500 ^{o}C in which they observed an enhancement of Al-interdiffusion in the alloy as the temperature increased.[27] In addition, another report showed that $Cu(In,Al)Se_2$ alloys only formed at

temperatures above 480 °C, preceded by the formation of $CuInSe_2$.[28] Therefore, although the detected peak from DSC was considerably weak, we speculate the endothermic process could be due to the release of the heat from partial formation of $Cu(In,Al)S_2$ alloy under the experimental conditions used during TG-DSC analysis.

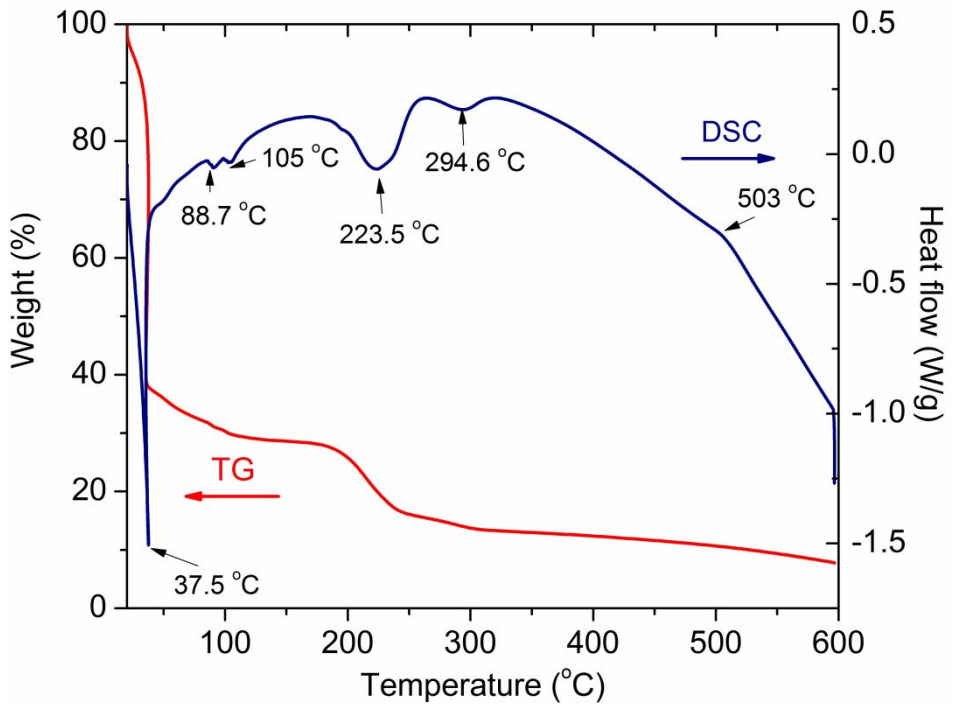

Figure 1. TG-DSC of ink made from CuCl-$InCl_3$-$AlNO_3$-thiourea dissolved in methanol under constant nitrogen gas flow (sample mass: 31.2 mg).

Figure 2a shows XRD spectra of as-deposited and selenized films fabricated with the Al-containing ink. The as-deposited film showed broad peaks at 27.79° and 46.61° assigned to (103) and (220/204) reflections of the chalcopyrite phase of $CuInS_2$, in agreement with its Raman spectrum (**Fig. S2**). The rather weak intensities imply that the as-deposited film had a low crystallinity. After selenization at 550 °C, the (103) and (220/204)-peaks measured on the absorber

made from ink containing aluminum (described as Al-CISSe) are left-shifted to 26.77° and 44.44° due to the replacement of the sulfur atoms with selenium. The peaks also become more intense as a result of grain growth during the high-temperature selenization process. The cross sectional SEM image presented in **Fig. S3a** of a 1.3 micron-thick Al-CISSe absorber confirms the high degree of crystallinity of the film after selenization, as evidenced by the size of the grains (up to 1 micron across) and the lack of void space. A 300-nm thick $MoSe_2$ layer, observed and measured in SEM imaging and detected in the XRD spectrum, was also formed due to partial selenization of the Mo substrate.

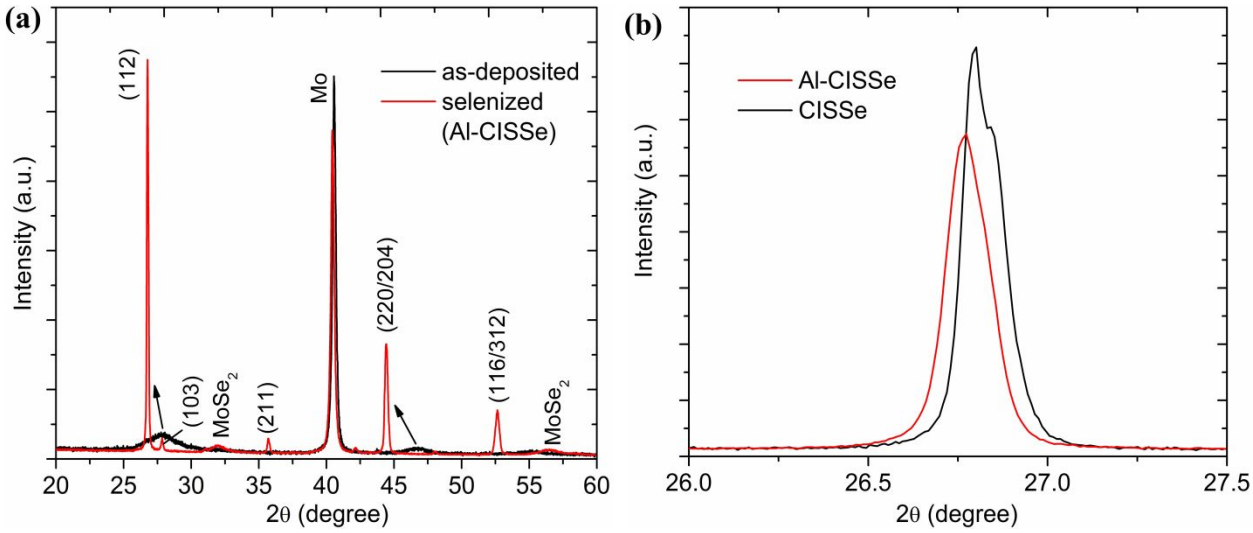

Figure 2. (a) XRD of as-deposited and selenized films fabricated with the Al-containing ink. (b) XRD spectrum at (112) peak from Al-CISSe and CISSe films.

To understand the effect of Al-incorporation to the chalcopyrite, (112)-orientation of the selenized film is compared in **Fig. 2b** to those fabricated from the Al-free ink (described as CISSe). In general, replacement of a heavier atom with a lighter one in the same group, in this case In with Al, would induce a shift toward a higher angle due to a shrinkage of the lattice.[28-30] However, a

small shift of the peak toward a lower angle was observed for Al-CISSe (2θ: 26.77°) relative to CISSe (2θ: 26.79°). The absence of any right shift in the XRD spectra could indicate negligible Al-alloying in CISSe. Based on AES analysis (**Fig. 3**), the Se/(S+Se) ratio of Al-CISSe and CISSe in the bulk were 0.91 and 0.90, respectively. As a reference, the (112) peak of $CuInSe_2$ and $CuInS_2$ are located at 2θ of 26.65° (JCPDS 87-2265) and 27.86 ° (JCPDS 65-2732), respectively. Therefore, assuming a linear relation between Se/(S+Se) ratio and the peak-shift on the $CuIn(S,Se)_2$ system following Vegard's law, Se/(S+Se) ratio of 0.91 and 0.90 would give a Δ2θ of 0.01°, a value very close to the one measured from XRD (0.02°). Although the values being compared are small, we conclude the 0.02° left-peak shift is most probably due to the slightly higher selenium content in the Al-CISSe, ruling out alloying of aluminum in CISSe to form $Cu(In,Al)Se_2$ in our experiment.

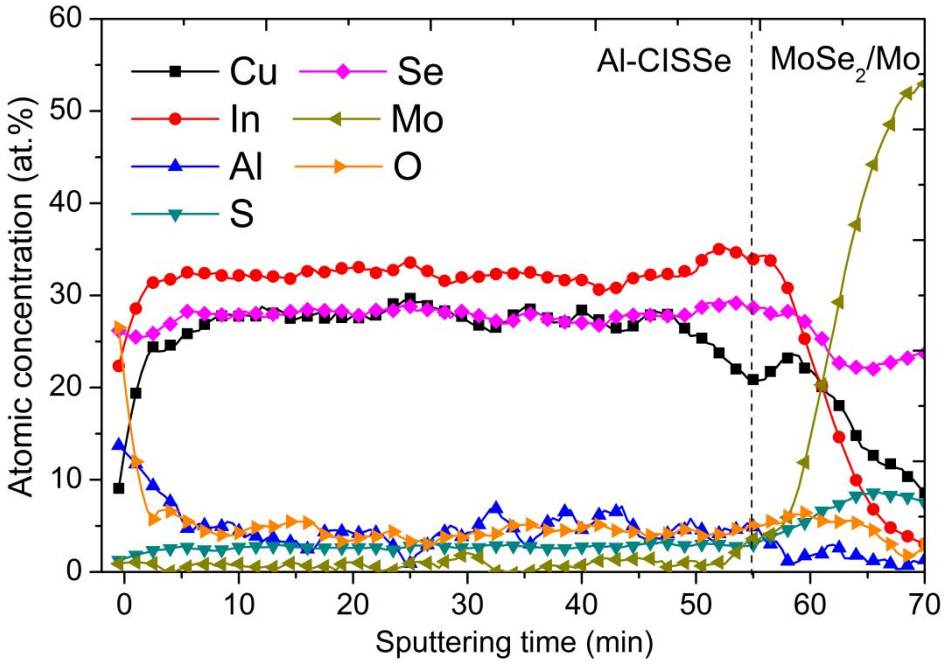

Figure 3. AES depth profiling of Al-CISSe. The bulk Al-CISSe film has average ratios of Cu/(Al+In): 0.75, Al/(Al+In): 0.12, Se/(S+Se): 0.91, as estimated from the AES spectra (sputtering time of 5 to 50 min).

The AES spectrum of the Al-CISSe also shows that Al is distributed throughout the film with an Al-rich composition observed at the surface. The ratio of Al/(Al+In) in the bulk is estimated to be 0.12 which is close to the intended ratio from the ink (~0.1). Oxygen at the surface observed for both Al-CISSe (**Fig. 3**) and CISSe (**Fig. S4**) might come partially from residual organic adsorbates during sample handling. It is worth noting that the increase in [O] at the surface of Al-CISSe coincides with an increase in [Al], and a substantial amount of [O] remains throughout the bulk of the film. In contrast, the CISSe film had a negligible [O] content in the bulk (**Fig. S4**). While metallic-Al is highly unlikely to form in our process, Al-O containing compounds such as Al_2O_3 or $Al(OH)_3$ could be formed during either the spin coating of the film (from the reaction of Al-salt with residual water in the ink) or during the hot plate annealing step (performed in air). Indeed, EDX mapping of the Al-CISSe film confirmed the presence of AlO_x grains at the surface and the bulk (**Fig. S5**).

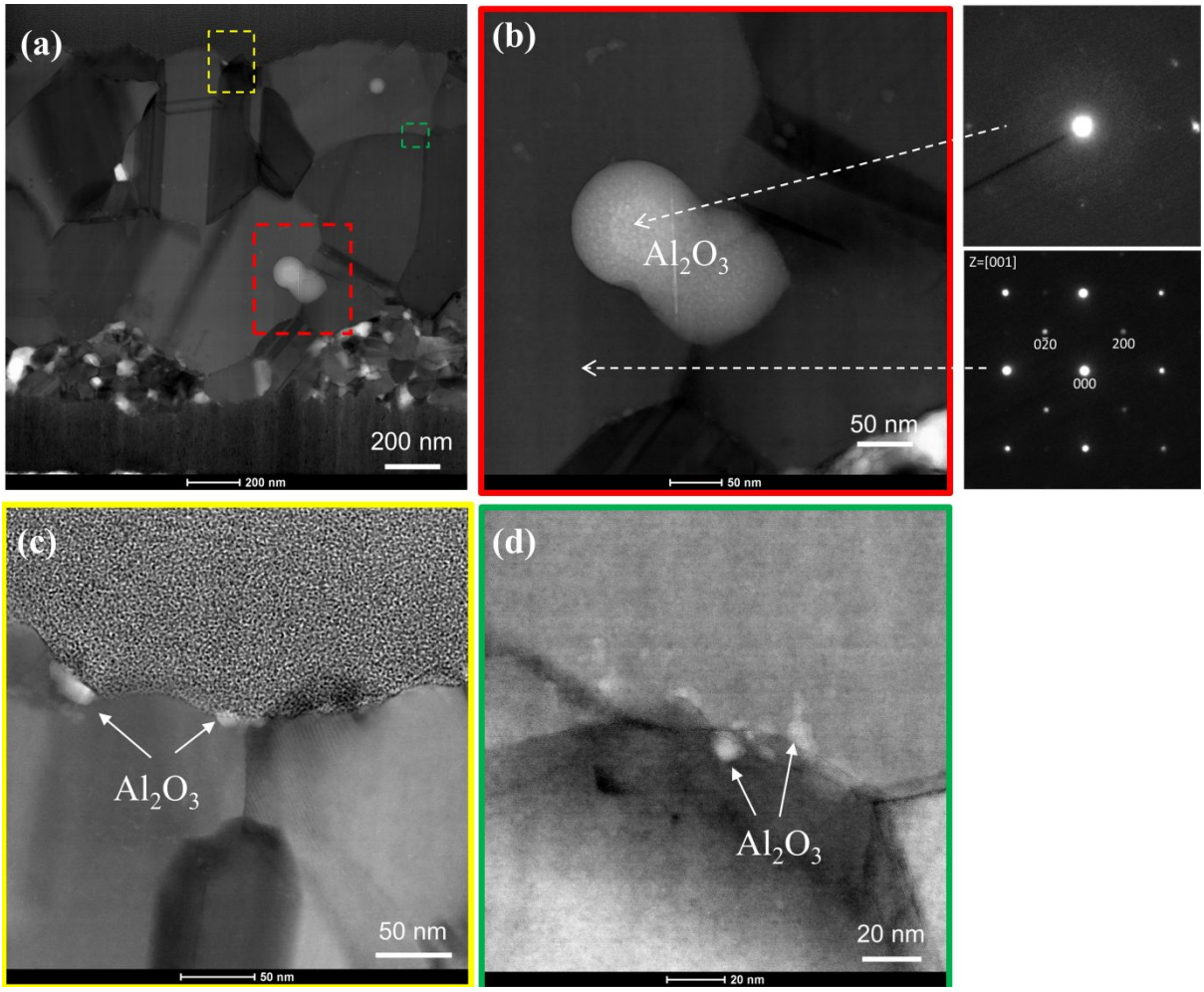

Figure 4. Bright-field (BF) STEM images taken from multiple areas on the Al-CISSe film: (a) entire cross-section of film, (b) grain interior, (c) near-surface and (d) grain boundaries within film. Insets at Fig. 4b show electron diffraction patterns from the bright spot and surrounding material. The bright spot has an Al/O atomic ratio of 0.65, which is very close to the ratio of stoichiometric Al_2O_3 (Al/O: 0.67).

The Al-CISSe sample were examined by TEM to further characterize AlO_x species in the selenized films (**Fig. 4**). The STEM-BF image in **Fig. 4a** reveals several bright spots dispersed throughout the film, suggesting the presence of different compounds other than CISSe. These bright spots are particularly obvious at the bottom area of the CISSe film where smaller grains formed (**Fig. S6**).

These segregated compounds were found to be as big as ~200 nm across, as evident in **Fig. 4b**. A point EDX analysis performed in the bright region in **Fig. 4b** revealed an Al/O atomic-ratio of 0.65, a value very close to stoichiometric Al_2O_3 (Al/O: 0.67). An electron diffraction pattern performed on the same bright spot shows a halo ring feature, revealing the lack of long-range ordering. In contrast, well-defined diffraction spots were observed on the CISSe grain next to the bright spot (dark region in **Fig 4b**). Therefore, we conclude that the Al-CISSe films fabricated with our molecular ink process are made of highly crystalline CISSe with isolated amorphous Al_2O_3 grains dispersed throughout. The amorphous nature of the Al_2O_3 explains the absence of any additional compounds other than chalcopyrite detected in the XRD (**Fig. 2a**) and Raman (**Fig. S2**) analyses. Higher magnification images reveal the presence of nanometer sized amorphous Al_2O_3 (~3-15 nm) covering parts of the absorber top surface (**Fig. 4c**) as well as at the grain boundaries (**Fig. 4d**). The detection of both aluminum and oxygen throughout the bulk by AES implies that nano-scale amorphous Al_2O_3 is present over the entirety of the Al-CISSe film, although only few remarkable spots are observed in the TEM micrograph.

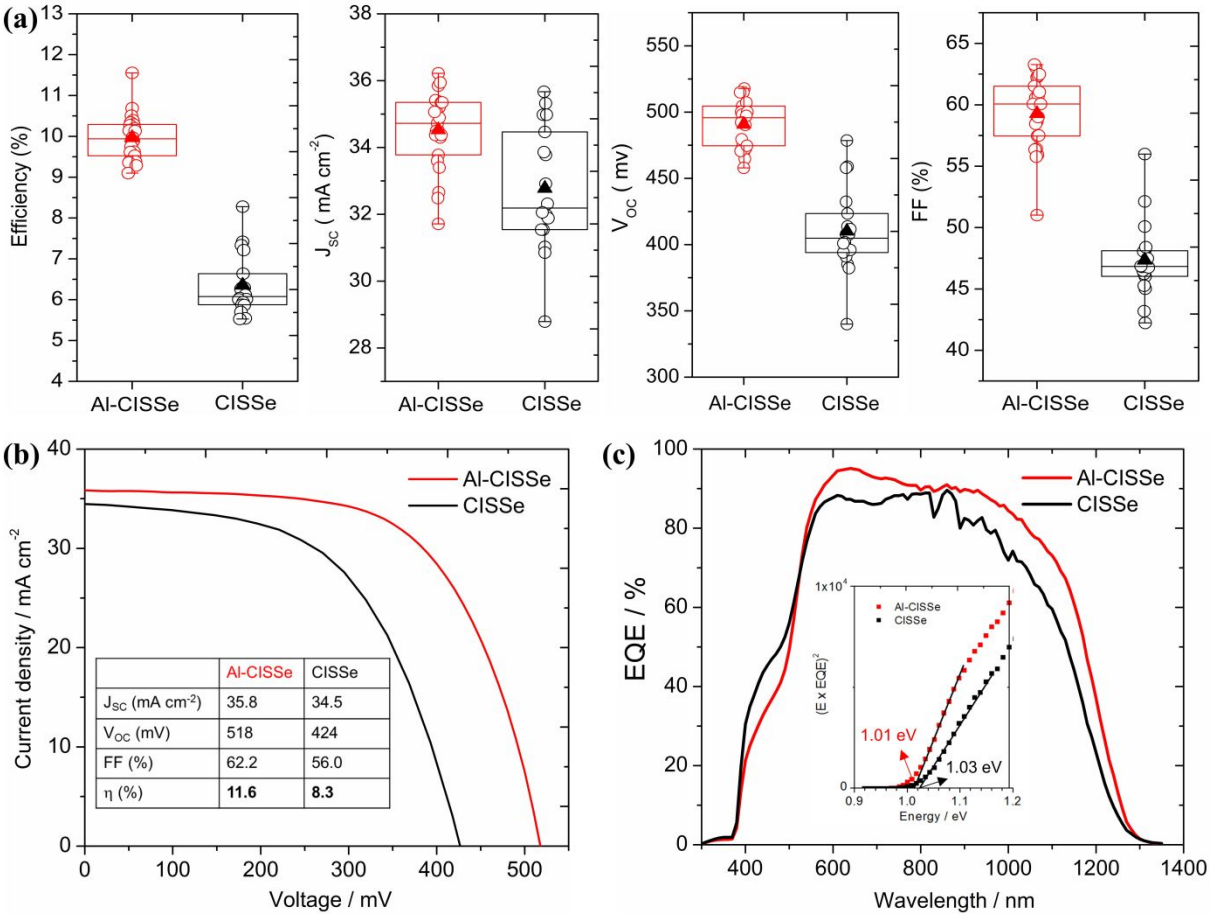

Figure 5. (a) Statistical box charts illustrating distribution of photovoltaic properties of Al-CISSe (total number of devices: 22) and CISSe (total number of devices: 18) solar cells. Filled triangles indicate average values. (b) Photocurrent density-voltage curves measured on Al-CISSe and CISSe champion cells. (c) EQE spectra of Al-CISSe and CISSe champion cells (inset shows estimation of band gaps). The J_{SC} integrated from EQE are 36.4 mA cm^{-2} and 34.0 mA cm^{-2} for Al-CISSe and CISSe cells, respectively.

Photovoltaic devices were then fabricated by chemical bath deposition of a CdS layer onto the absorbers, followed by sputtering of a ZnO/ITO bilayer. **Figure 5a** shows the statistical distribution of photovoltaic performances from the Al-CISSe solar cells fabricated from multiple batches (total number of devices: 22). Photovoltaic performance of CISSe solar cells fabricated

through similar methods are also shown for comparison (total number of devices: 18). Overall, PCE of Al-CISSe devices are consistently higher than that of CISSe. Al-CISSe devices had PCE ranging from 9.1% to a maximum efficiency of 11.6% (champion Al-CISSe cell: J_{SC} = 35.8 mA cm^{-2}, V_{OC} = 518 mV, FF = 62.2%, no anti reflective coating) with an average PCE of 10.1%, whereas CISSe devices showed PCE from 5.5% to a maximum of 8.3% (champion CISSe cell: J_{SC} = 34.5 mA cm^{-2}, V_{OC} = 424 mV, FF = 56.0%) and an average PCE of 6.4%. Figure 5b shows the photocurrent density-voltage curves from the champion Al-CISSe and CISSe devices. Shunt resistances (R_{Sh}), estimated using a one-diode model, were three times higher in Al-CISSe (428.3 $\Omega.cm^2$) compared to CISSe (125.1 $\Omega.cm^2$), whereas series resistances were found to be relatively comparable (3.6 $\Omega.cm^2$ and 2.8 $\Omega.cm^2$ for CISSe and Al-CISSe, respectively). The average J_{SC} of Al-CISSe devices (34.5 mA cm^{-2}) was found to be slightly higher compared to that of the CISSe devices (32.8 mA cm^{-2}), as seen from the increased EQE in almost entire wavelength range (**Fig. 5c**). The electronic (as measured by EQE) and optical (as measured by diffuse reflectance, **Fig. S7**) bandgaps of Al-CISSe (E_{EQE} = 1.01 eV, $E_{reflec.}$= 1.01 eV) and CISSe (E_{EQE} = 1.03 eV, $E_{reflec.}$= 1.01 eV) where found to be nearly identical, confirming that Al does not alloy with CISSe to form $Cu(In,Al)Se_2$ in our experiment.

The Al-CISSe devices had significantly superior V_{OC} (<V_{OC}(Al:CISSe)>/<V_{OC}(CISSe)>=1.2) and FF (<FF>(Al:CISSe)/<FF>(CISSe)=1.26) compared to CISSe devices, as expected from the appreciably higher R_{Sh}. We speculate that Al_2O_3 plays a role in the enhancement of the photovoltaic properties by passivating defects and reducing interface recombination, as already reported on other thin film materials coated with Al_2O_3 layers either at the top or the back interface (CIGSe,[4,5] CZTSe,[11,12] CdTe[13,14]). With our approach, nanometer-sized amorphous Al_2O_3 is present not only

at the top and bottom interfaces of CISSe (**Fig. 4a and 4c**), but also in the film bulk and at grain boundaries (**Fig. 4d**).

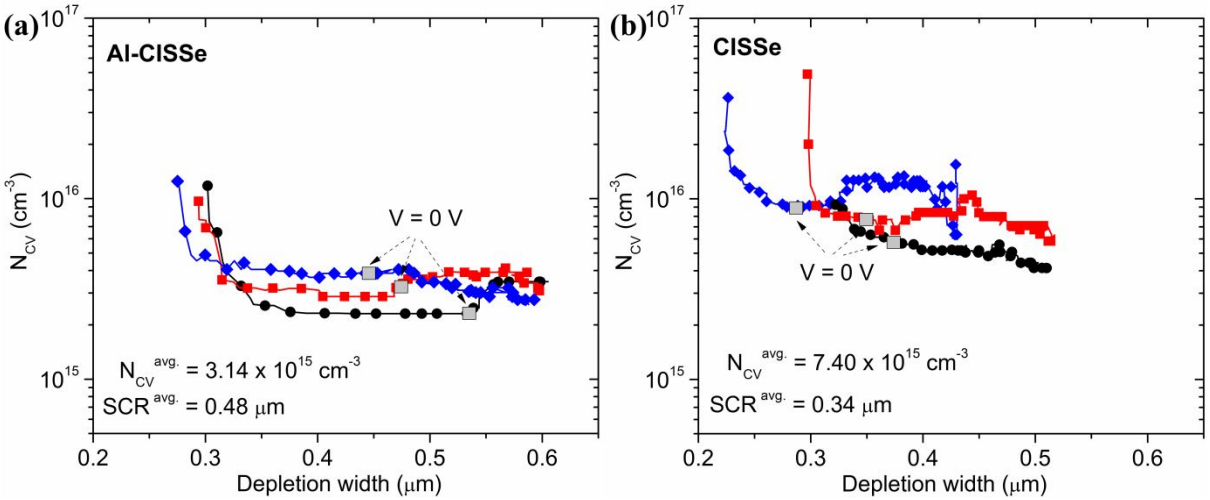

Figure 6. Comparison of depth profiles of apparent doping density (N_{CV}) deduced from C-V measurements of (a) three Al-CISSe and (b) three CISSe solar cells. Gray filled squares indicate V = 0 V. Average of N_{CV} and space charge region (SCR) at 0 V are calculated to be 3.14 x 10^{15} cm^{-3} and 0.48 μm for Al-CISSe, and 7.40 x 10^{15} cm^{-3} and 0.34 μm for CISSe.

To confirm our hypothesis on the passivation of CISSe with in-situ incorporated Al_2O_3, C-V measurements were carried out on three Al-CISSe and three CISSe devices. Figure 6 shows the apparent doping density (N_{CV}) vs. depletion width extracted according to methods reported in the literature.[31] It is can be observed that Al-CISSe devices have lower N_{CV} compared to CISSe. At 0 V, the average N_{CV} of Al-CISSe was estimated to be 3.14 x 10^{15} cm^{-3}, while the CISSe devices had an average N_{CV} of 7.40 x 10^{15} cm^{-3}. Since bulk and interface defects are responsive to C-V measurement,[31] the lower N_{CV} of Al-CISSe implies a reduced overall defect density of CISSe with the presence of Al_2O_3. Previous reports on ALD-Al_2O_3 passivated CIGSe and CZTSSe solar cells

also showed reduced doping density from C-V measurements consistent with our results.[32-34] Apart from the reduced defect density, the space charge region (SCR) is wider in Al-CISSe devices (average SCR = 0.48 μm) than that in CISSe devices (average SCR = 0.34 μm). This contributed to the increased EQE (see Fig. 5c) and therefore the J_{SC} of Al-CISSe devices.[32,35] Since the Al_2O_3 was detected throughout the absorber, we conclude that the extended SCR is a direct indicator of the passivation of defects in the CISSe bulk.

In addition, the relatively low doping density in Al-CISSe suggests that Cd (from CdS) is allowed to diffuse into CISSe despite the presence of Al_2O_3. It is known that some extent of Cd and/or Zn inter-diffusions in CIGSe cells are favorable to lower the doping (from ~10^{17} cm^{-3} to ~10^{15}-10^{16} cm^{-3}), leading to wider SCR.[36-38] However, a recent study by Werner et al. on CIGSe coated with ALD-Al_2O_3 suggest that an exceedingly thick Al_2O_3 passivation layer prevents Cd and Zn diffusions.[38] As such, CIGSe with a high doping density (in the range of 10^{17} cm^{-3}) was obtained when coated with 20nm-thick Al_2O_3, while coating the CIGSe with ultra-thin Al_2O_3 (~1 nm) resulted in doping density of 10^{16} cm^{-3}. In our case, Al_2O_3 nano-particles can be rather large, yet they are sparsely dispersed on the CISSe top and bottom surface and the bulk, as seen in **Fig. 4**. We speculate that this feature allowed Cd to diffuse into the uncoated regions of CISSe sub-surface. Therefore, we hypothesize that the localized nature of Al_2O_3 formed with our approach allowed the CISSe films to have doping density optimal for charge collection and, at the same time, passivated defects, resulting in superior photovoltaic properties.

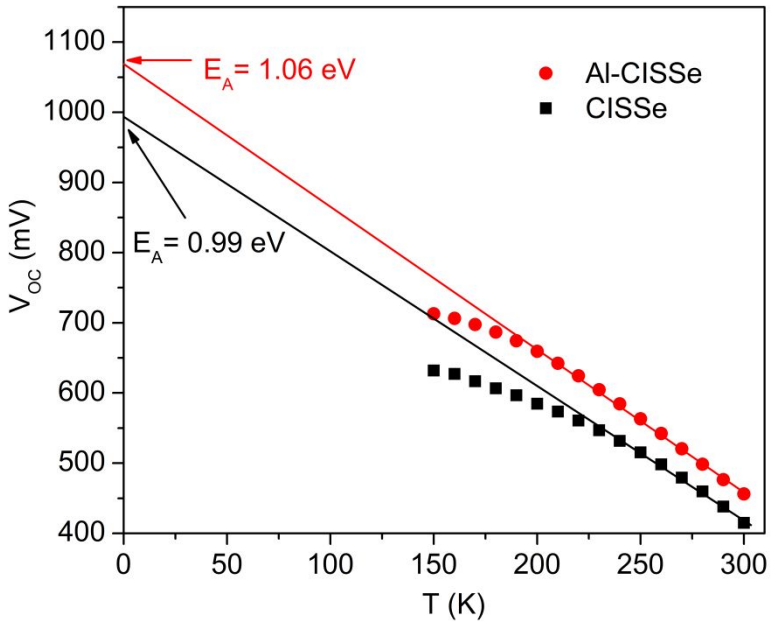

Figure 7. Temperature-dependent V_{OC} measurements performed on Al-CISSe and CISSe solar cells. Extrapolation of V_{OC} to 0 K gives the activation energy (E_A).

Finally, the activation energy (E_A) of the dominant recombination mechanism in Al-CISSe (PCE = 9.47%, J_{SC} = 32.5 mA cm^{-2}, V_{OC} = 479 mV, FF = 63.05%) and CISSe (PCE = 6.19%, J_{SC} = 31.5 mA cm^{-2}, V_{OC} = 429 mV, FF = 47.50%) devices was investigated via V_{OC}-T measurements. These values were estimated by extrapolating the linear portion of V_{OC}-T in the high temperature region to 0 K.[39] As presented in **Figure 7,** a difference of 70 mV in activation energy was observed between Al-CISSe (E_A = 1.06 eV) and CISSe (E_A = 0.99 eV), indicating that interface recombination is more severe in the CISSe devices than it is in the Al-CISSe devices. Using the results obtained from both V_{OC}-T and C-V measurements, we conclude our in-situ Al_2O_3 incorporation process reduces defect density in the absorber (as evidenced by a widening of SCR) as well as at the junction with CdS (as demonstrated by an increase in E_A).

4. Conclusion

We report a fabrication of CISSe thin film incorporated with amorphous Al_2O_3 by selenization of spin coated precursor film prepared from a molecular ink containing salts of Cu, In, Al, and thiourea dissolved in methanol. XRD, AES and TEM analyses of the film showed that amorphous Al_2O_3 were sparsely formed on the top and bottom surfaces and at bulk and grain boundaries of CISSe. The solar cell fabricated from such film had a maximum efficiency of 11.6% without anti-reflection, a value significantly higher than that of solar cells made from the ink without the addition of Al. The improvements stemmed primarily from increased V_{OC} as well as FF. Defect passivation via in-situ formed Al_2O_3 is thought to play a major role in the improvement of the solar cell performance through decreased interface and bulk recombination. Future efforts will be focused on increasing the concentration and dispersion of Al_2O_3 in CISSe with our in-situ method to further reduce defect densities and improve efficiency. Complementary analysis is required to conclude if the mechanism reported on ALD-coated Al_2O_3 layers applies also to nanoparticles as created with our in-situ approach. Nevertheless, this promising in-situ passivation approach could be extended to other chalcogenide materials synthesized by the molecular-ink approach.

Conflict of Interest

There are no conflicts to declare.

Acknowledgement

This work was funded by the U.S. Department of Energy under contract DE-EE0008085 and the Office of Naval Research Asia Pacific Research Initiative for Sustainable Energy Systems

(APRISES) under contract N00014-19-1-2159. The authors acknowledge the assistance of Dr. Godwin Severa for the TG-DSC measurement. The authors would also like to thank Dr. Przemyslaw Dera for his assistance in the XRD measurement. This work was authored in part by the National Renewable Energy Laboratory, operated by Alliance for Sustainable Energy, LLC, for the U.S. Department of Energy (DOE) under Contract No. DE-AC36-08GO28308. Funding provided by the U.S. Department of Energy, Office of Energy Efficiency and Renewable Energy, Hydrogen and Fuel Cell Technology Office. The views expressed in the article do not necessarily represent the views of the DOE or the U.S. Government. The U.S. Government retains and the publisher, by accepting the article for publication, acknowledges that the U.S. Government retains a nonexclusive, paid-up, irrevocable, worldwide license to publish or reproduce the published form of this work, or allow others to do so, for U.S. Government purposes.

References

[1] Solar Frontier press release, http://www.solar-frontier.com/eng/news/2019/0117_press.html (accessed: December 2020).

[2] M. Nakamura, K. Yamaguchi, Y. Kimoto, Y. Yasaki, T. Kato, H. Sugimoto, *IEEE J. Photovolt.*, 2019, **9**, 1863.

[3] Fraunhofer ISE photovoltaics report, https://www.ise.fraunhofer.de/content/dam/ise/de/documents/publications/studies/Photovoltaics-Report.pdf (accessed: January 2021)

[4] J. Cunha, P. Fernandes, A. Hultqvist, J. Teixeira, S. Bose, B. Vermang, S. Garud, D. Buldu, J. Gaspar and M. Edoff, *IEEE J. Photovolt.*, 2018, **8**, 1313.

[5] M. Curado, J. Teixeira, M. Monteiro, E. Ribeiro, R. Vilão, H. Alberto, J. Cunha, T. Lopes, K. Oliveira and O. Donzel-Gargand, *Appl. Mater. Today*, 2020, **21**, 100867.

[6] W.-W. Hsu, J. Chen, T.-H. Cheng, S. Lu, W.-S. Ho, Y.-Y. Chen, Y.-J. Chien and C. Liu, *Appl. Phys. Lett.,* 2012, **100**, 023508.

[7] R. Kotipalli, B. Vermang, J. Joel, R. Rajkumar, M. Edoff and D. Flandre, *AIP Adv.*, 2015, **5**,107101.

[8] F. Werner, B. Veith-Wolf, C. Spindler, M.R. Barget, F. Babbe, J. Guillot, J. Schmidt and S. Siebentritt, *Phys. Rev. Appl.*, 2020, **13**, 054004.

[9] J. Schmidt, A. Merkle, R. Brendel, B. Hoex, M.v. de Sanden and W. Kessels, *Prog. Photovolt.*, 2008, **16**, 461-466.

[10] G. Dingemans and W. Kessels, *J. Vac. Sci. Technol. A*, 2012, **30**, 040802.

[11] J. Park, J. Huang, J. Yun, F. Liu, Z. Ouyang, H. Sun, C. Yan, K. Sun, K. Kim and J. Seidel, *Adv. Energy Mater.*, 2018, **8**, 1701940.

[12] Y.S. Lee, T. Gershon, T.K. Todorov, W. Wang, M.T. Winkler, M. Hopstaken, O. Gunawan and J. Kim, *Adv. Energy Mater.*, 2016, **6**, 1600198.

[13] J.M. Kephart, A. Kindvall, D. Williams, D. Kuciauskas, P. Dippo, A. Munshi and W. Sampath, *IEEE J. Photovolt.*, 2018, **8**, 587.

[14] G. Zeng, X. Hao, S. Ren, L. Feng and Q. Wang, *Energies*, 2019, **12**, 1123.

[15] B. Hoex, S. Heil, E. Langereis, M. Van de Sanden and W. Kessels, *Appl. Phys. Lett.*, 2006, **89**, 042112.

[16] F. Werner, B. Veith, D. Zielke, L. Kühnemund, C. Tegenkamp, M. Seibt, R. Brendel and J. Schmidt, *J. Appl. Phys.*, 2011, **109**, 113701.

[17] D.K. Simon, P.M. Jordan, T. Mikolajick and I. Dirnstorfer, *ACS Appl. Mater. Interfaces*, 2015, **7**, 28215.

[18] N. Terlinden, G. Dingemans, M.M. van de Sanden and W. Kessels, *Appl. Phys. Lett.*, 2010, **96**, 112101.

[19] G. Dingemans, N. Terlinden, D. Pierreux, H. Profijt, M. Van de Sanden and W. Kessels, *Electrochem. Solid-State Lett.*, 2010, **14**, H1.

[20] C.L. Perkins, B. Egaas, I. Repins and B. To, *Appl. Surf. Sci.*, 2010, **257**, 878.

[21] J. Madarász and G. Pokol, *J. Therm. Anal. Calorim.*, 2007, **88**, 329.

[22] S. Wang, Q. Gao and J. Wang, *J. Phys. Chem. B*, 2005, **109**, 17281.

[23] M. Krunks, T. Leskelä and L. Niinistö, *Jpn. J. Appl. Phys.,* 2000, **39**, 181.

[24] A.R. Uhl, A. Rajagopal, J.A. Clark, A. Murray, T. Feurer, S. Buecheler, A.K.Y. Jen and H.W. Hillhouse, *Adv. Energy Mater.*, 2018, **8**, 1801254.

[25] A.R. Uhl, J.K. Katahara and H.W. Hillhouse, *Energy Environ. Sci.*, 2016, **9**, 130.

[26] K. Otto, P. Bombicz, J. Madarász, I. Oja Acik, M. Krunks and G. Pokol, *J. Therm. Anal. Calorim.*, 2011, **105**, 83.

[27] R.K. Bhandari, Y. Hashimoto and K. Ito, *Jpn. J. Appl. Phys.*, 2006, 45, 8592.

[28] S. Jost, F. Hergert, R. Hock, M. Purwins and R. Enderle, *Phys. Status Solidi A*, 2006, **203**, 2581.

[29] J. Olejníček, C. Kamler, S.A. Darveau, C. Exstrom, L. Slaymaker, A. Vandeventer, N. Ianno and R. Soukup, *Thin Solid Films*, 2011, **519**, 5329.

[30] J. Olejníček, L. Flannery, S.A. Darveau, C. Exstrom, Š. Kment, N. Ianno and R. Soukup, *J. Alloys Compd.*, 2011, **509**, 10020.

[31] J.T. Heath, J.D. Cohen and W.N. Shafarman, *J. Appl. Phys.*, 2004, **95**, 1000.

[32] J. Keller, F. Gustavsson, L. Stolt, M. Edoff and T. Törndahl, *Sol. Energy Mater Sol. Cells*, 2017, **159**, 189.

[33] M.E. Erkan, V. Chawla and M.A. Scarpulla, *J. Appl. Phys.*, 2016, **119**, 194504.

[34] X. Cui, K. Sun, J. Huang, J.S. Yun, C.-Y. Lee, C. Yan, H. Sun, Y. Zhang, C. Xue and K. Eder, *Energy Environ. Sci.*, 2019, **12**, 2751.

[35] N. Valdes, J.W. Lee, W. Shafarman, *Sol. Energy Mater Sol. Cells*, 2019, **195**, 155.

[36] U. Rau and M. Schmidt, *Thin Solid Films*, 2001, **387**, 141.

[37] F. Werner, F. Babbe, J. Burkhart, C. Spindler, H. Elanzeery and S. Siebentritt, *ACS Appl. Mater. Interfaces*, 2018, **10**, 28553.

[38] F. Werner, B. Veith-Wolf, M. Melchiorre, F. Babbe, J. Schmidt and S. Siebentritt, *Sci. Rep-Uk*, 2020, **10**, 1.

[39] M. Turcu, O. Pakma and U. Rau, *Appl. Phys. Lett.*, 2002, **80**, 2598.